Photocatalytic degradation of methyl orange by $Bi_{20}TiO_{32}$–montmorillonite composite

Haichun Xiang[1,2], *Biyang Tuo*[1,2,3] ✉, *Xiang Song*[1,2]

[1]*College of Mining, Guizhou University, Guiyang 550025, People's Republic of China*
[2]*GuiZhou Key Laboratory of Comprehensive Utilization of Non-metallic mineral resources, Guiyang 550025, People's Republic of China*
[3]*National & Local Joint Laboratory of Engineering for Effective Utilization of Regional Mineral Resources from Karst Areas, Guiyang 550025, People's Republic of China*
✉ *E-mail: yntby@163.com*

Published in Micro & Nano Letters; Received on 25th February 2020; Revised on 2nd April 2020; Accepted on 6th April 2020

To solve the problem of methyl orange (MO) dye wastewater pollution, TiO_2–montmorillonite composite (TiO_2–MMT) and $Bi_{20}TiO_{32}$–montmorillonite composite ($Bi_{20}TiO_{32}$–MMT) were synthesised by the sol–gel method, and they were used for photocatalytic degradation of MO solution. The results showed that TiO_2 in TiO_2–MMT existed as the anatase type, and $Bi_{20}TiO_{32}$ in $Bi_{20}TiO_{32}$–MMT existed as the tetragonal crystal type. When the dosage of the composite was 0.50 g/l, the initial concentration of the MO solution was 20 mg/l, and the pH was 3, the decolourisation rate of MO solution using TiO_2–MMT treating was 87.11%, and it reached 98.50% after $Bi_{20}TiO_{32}$–MMT treating. When $Bi_{20}TiO_{32}$–MMT was reused four times, the decolourisation rate of the MO solution was only reduced by 3.5%. The photocatalytic degradation between MO solution and $Bi_{20}TiO_{32}$–MMT complied with the pseudo-first-order kinetic equation. Holes and superoxide radicals interacted directly with MO during photocatalytic degradation, which reduced the probability of hole–electron recombination, and improved the photocatalytic degradation property of $Bi_{20}TiO_{32}$–MMT. $Bi_{20}TiO_{32}$–MMT has excellent stability property, which makes it a good composite in the treatment of dye wastewater.

1. Introduction: Azobenzene sulphonic acid dye wastewater is characterised by large chroma, complex composition, and high concentration of organic pollutants, which makes it difficult to treat [1, 2]. When dye wastewater discharges into water, it will consume dissolved oxygen, disrupt the ecological balance of water, and endanger the survival of water [3]. How to treat dye wastewater efficiently is an urgent problem. Common methods to treat dye wastewater include coagulation, adsorption, membrane separation technology, and semiconductor photocatalytic degradation technology [4–7]. The characteristics of semiconductor photocatalytic degradation technology are of high efficiency, low energy consumption, and using light energy to oxidise and decompose organic substances at room temperature, which has caused widespread attention [8].

TiO_2 has been extensively studied due to its low cost, non-toxicity, high activity, and excellent stability [9, 10]. However, its wide bandgap and high hole–electron recombination rate limit its application. To improve the photocatalytic activity of TiO_2, it is necessary to study the modification of TiO_2 [11–13]. TiO_2 and Bi_2O_3 can be combined to form bismuth titanate compounds with various crystal phase structures including $Bi_2Ti_2O_7$ (2.82 eV) [14], $Bi_4Ti_3O_{12}$ (2.79 eV) [15], $Bi_{12}TiO_{20}$ (2.65 eV) [16], $Bi_{20}TiO_{32}$ (2.38 eV) [17], and so forth. They have excellent photocatalytic performance. At present, there are lot of research studies on $Bi_2Ti_2O_7$, $Bi_4Ti_3O_{12}$, and $Bi_{12}TiO_{20}$. For example, Lomanova has studied the co-precipitation method to synthesise bismuth titanate nanocrystals (Bi_2Ti4O_{11}, $Bi_4Ti_3O_{12}$, $Bi_2Ti_2O_7$ etc.). The result showed that the grain size of the material is determined by the minimum grain size of the first phase crystallised in the reaction system. The material synthesis and sintering process parameters are related to the melting point of the surface (non-spontaneous) phase [18]. Kumar has studied two different methods for preparing $Bi_2Ti_2O_7$ nano-powder. The result shows that compared with the co-precipitation method, the nano-powder synthesised by the Pechini method exhibits higher photocatalytic activity under ultraviolet (UV) light irradiation [19]. Fang has synthesised single-phase $Bi_4Ti_3O_{12}$ and $Bi_{12}TiO_{20}$ particles with well crystal shapes by a rapid microwave-assisted sol–gel method. The result shows that rapid sintering with a microwave can effectively increase the specific surface area of the obtained bismuth titanate [20]. However, there are few studies on $Bi_{20}TiO_{32}$ because it is difficult to get a single-phase and high crystallinity. Also, the research of $Bi_{20}TiO_{32}$–montmorillonite composite ($Bi_{20}TiO_{32}$–MMT) has not been reported in the literature.

Montmorillonite, as a layered silicate mineral, is negatively charged on the surface and has good expansibility, adsorption, and ion exchange properties [21]. It is an excellent carrier material for improving the stability and activity of photocatalyst. In this Letter, TiO_2–montmorillonite composite (TiO_2–MMT) and $Bi_{20}TiO_{32}$–MMT were prepared by the sol–gel method using sodium montmorillonite (Na–MMT) as a carrier. X-ray diffraction (XRD), SEM, energy dispersion spectroscopy (EDS), and UV–visible diffuse reflectance spectroscopy (UV–Vis DRS) were used to analyse three composites. The photocatalytic degradation performance and photocatalytic mechanism of composites were discussed using the methyl orange (MO) solution as the target pollutant.

2. Experimental

2.1. Materials: Calcium montmorillonite was provided by Chifeng Hengrun Industry and Trade Co., Ltd (China). Tetrabutyl titanate, bismuth nitrate pentahydrate, sodium hexametaphosphate, ethanol, acetic acid, nitric acid, sodium hydroxide, and MO were purchased from Sinopharm Chemical Reagent Co., Ltd (China). All chemicals were of analytical grade and used directly without further purification.

2.2. Synthesis of composites: Na–MMT was chosen as a composite carrier. Its synthesis method is detailed in [22]. 10 ml tetrabutyl titanate, 10 ml ethanol, and 2 ml acetic acid were mixed, and the pH was adjusted to 6 with sodium hydroxide (2 mol/l) to obtain a precursor solution. The precursor solution was added to the

Na–MMT suspension (2.6% by mass), magnetically stirred for 30 min, aged for 1 h, and then centrifuged. The obtained solid was washed with distilled water, dried, ground, and calcined at 673 K for 1 h to synthesise TiO_2–MMT.

The synthesis difference between $Bi_{20}TiO_{32}$–MMT and TiO_2–MMT was mainly reflected in different precursor solutions. 4.90 g of bismuth nitrate pentahydrate was mixed with nitric acid (2 mol/l). The mixed solution was added to the precursor solution of TiO_2–MMT. The pH was adjusted to 6 to obtain a precursor solution.

2.3. Characterisation of composites: XRD was used to detect the crystal structure of composites, copper target, and the scanning angle (2θ) was 10°–80° (X′Pert PRO, PANalytical, Netherlands). SEM was used to analyse the micro-morphology of three composites, and the components were analysed by the matching EDS (ZEISS MERLIN Compact, Zeiss, Germany). UV–Vis DRS was used to measure the light absorption properties of three composites, ranging from 200 to 800 nm (Lambda 750S, PERKI-NELMER, USA).

2.4. Adsorption study: Different composites (0.05 g) were added to 100 ml of MO solution (20 mg/l) and stirred in the dark for 40 min. 5 ml of the solution was taken every 5 min, and the absorbance was measured using an UV–Vis spectrophotometer (UV-Vis, TU-1901, China) at a wavelength of 465 nm. The adsorption amount of MO is calculated by the following equation:

$$q_t = \frac{(C - C_t)V}{W} \tag{1}$$

where q_t is the adsorption capacity at time t, mg/g; C is the initial concentration of MO solution, mg/l; C_t is the concentration of MO solution at time t; V is the initial volume of MO solution, l; W is the amount of composite, g.

2.5. Photocatalytic degradation test: The three kinds of composites (0.05 g) were separately put into a 100 ml MO solution with a particular initial concentration, and the pH was adjusted to 3, magnetically stirred in a dark box for 30 min to reach adsorption equilibrium. Then it was transferred under the UV lamp shining in the box and takes 5 ml of solution every 20 min. The absorbance of the solution was measured using a UV–Vis at a wavelength of 465 nm. The decolourisation rate of MO is calculated by the following equation:

$$\eta = \frac{C - C_t}{C} \tag{2}$$

where η is the decolourisation rate of MO, %; C is the initial concentration of MO solution, mg/l; C_t is the concentration of the MO solution after light irradiation for time t, mg/l.

3. Results and discussion

3.1. Characterisation of composites: The XRD patterns of Na–MMT, TiO_2–MMT, and $Bi_{20}TiO_{32}$–MMT are shown in Fig. 1. XRD pattern of Na–MMT shows diffraction peaks at 2θ of 19.9°, 34.9°, 36.1°, 54.1°, and 62.0°. Their diffraction peaks coincide with the standard card (JCPDS No. 13-0135). The peaks at 22.0° and 29.0° belong to quartz [23]. XRD pattern of TiO_2–MMT shows diffraction peaks at 2θ of 25.6°, 38.2°, 48.4°, 54.5°, and 62.8° are corresponding to (101), (004), (200), (211), and (204) crystal planes, respectively. It indicates that TiO_2 is the anatase phase [24]. Besides, the change in the diffraction peak of montmorillonite at 19.9° indicates that the crystallinity of montmorillonite has changed [25]. In the XRD pattern of $Bi_{20}TiO_{32}$–MMT, there is only one diffraction peak of TiO_2 belonging to the (101) crystal plane. This is because the size of Bi^{3+} ion (ionic radius

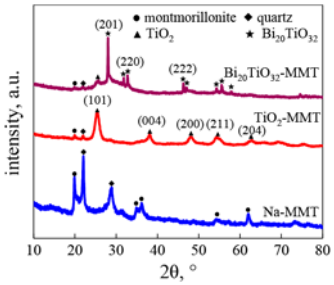

Fig. 1 *XRD patterns of Na–MMT, TiO_2–MMT, and $Bi_{20}TiO_{32}$–MMT*

103 pm) is bigger than Ti^{4+} ion (ionic radius 61 pm), which prevents Bi^{3+} from replacing Ti^{4+} in the TiO_2 crystal lattice [26]. Therefore, Bi_2O_3 is dispersed on the surface of TiO_2 and form a new phase with it. This inhibits the growth of TiO_2 [27–29]. The diffraction peaks of $Bi_{20}TiO_{32}$ with the tetragonal phase formed by the combination of Bi_2O_3 and TiO_2 are very sharp. The central peak ((201) crystal plane) is large and distinct, and the crystal planes at 32°, 46°, and 75° also grow well. It shows that $Bi_{20}TiO_{32}$ has good crystallinity.

The SEM images of Na–MMT, TiO_2–MMT, and $Bi_{20}TiO_{32}$–MMT are shown in Figs. 2*a–c*. It can be seen from Fig. 2*a*, Na–MMT has typical layered structures and smooth surfaces. In Fig. 2*b*, the morphology of TiO_2–MMT has changed significantly compared to Na–MMT. The phenomenon of lamella peeling appears, destroying the original structure of montmorillonite [30]. At the same time, TiO_2 round particles are loaded on montmorillonite. In Fig. 2*c*, as for $Bi_{20}TiO_{32}$–MMT, its layered structure has been partly destroyed, and round particles are loaded. Compared with TiO_2–MMT, the agglomeration between round particles is more serious. The main reason is that the surface electrical properties of $Bi_{20}TiO_{32}$ and TiO_2 particles are different, which results in different agglomeration phenomena between particles. Also, a small number of tapered particles appear in Fig. 2*c*. The tapered $Bi_{20}TiO_{32}$ was found, which was consistent with the tapered $Bi_{20}TiO_{32}$ found during the preparation of $Bi_2Ti_2O_7$ nanocrystals in the literature [31]. EDS was used to determine the chemical composition (Fig. 2*d*). Besides the peaks of Na, K, Mg, Al, P, and Si that belong to montmorillonite, the peaks of O, Ti, and Bi also appear. The formation of $Bi_{20}TiO_{32}$–MMT can be confirmed.

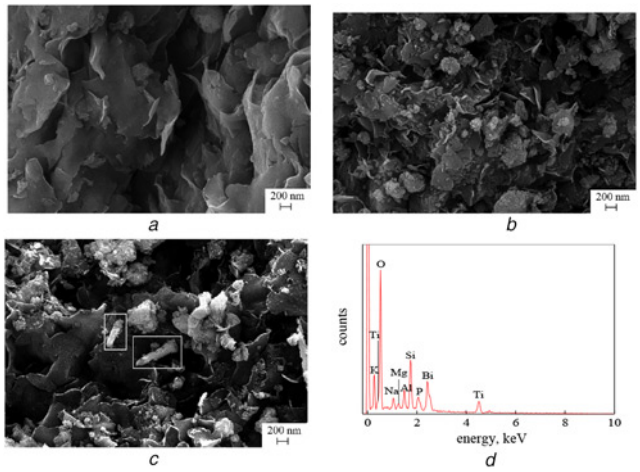

Fig. 2 *Morphology of composites and chemical composition of $Bi_{20}TiO_{32}$–MMT*
a–c SEM images of Na–MMT, TiO_2–MMT, and $Bi_{20}TiO_{32}$–MMT
d EDS spectrum of $Bi_{20}TiO_{32}$–MMT

doi: 10.1049/mnl.2020.0127

The light absorption properties of Na–MMT, TiO_2–MMT, and $Bi_{20}TiO_{32}$–MMT are shown in Fig. 3. Three kinds of composites can absorb UV and visible light, and their light absorption edges are located at 359, 393, and 514 nm, respectively. The bandgap of three composites is calculated according to the following equation [32, 33]:

$$E_g = 1240/\lambda_g \tag{3}$$

where E_g is the bandgap (eV) and λ_g is the light absorption edge (nm).

TiO_2–MMT has a bandgap of 3.16 eV, which is lower than that of pure anatase TiO_2 (3.2 eV). It is because the presence of montmorillonite reduces the bandgap and improves the photocatalytic activity [34]. The redshift of the absorption band for $Bi_{20}TiO_{32}$–MMT is observed, and its bandgap is 2.41 eV, which has higher photocatalytic activity.

3.2. Adsorption study: Fig. 4 shows the effect of contact time on the adsorption of MO by Na–MMT, TiO_2–MMT, and $Bi_{20}TiO_{32}$–MMT. TiO_2–MMT and $Bi_{20}TiO_{32}$–MMT both adsorbed MO more than Na–MMT. It shows that TiO_2 or $Bi_{20}TiO_{32}$ particles enter the interlayer of montmorillonite and increase the interlayer distance. However, the agglomeration of $Bi_{20}TiO_{32}$ particles is more serious, which makes the adsorption amount of $Bi_{20}TiO_{32}$–MMT lower than that of TiO_2–MMT. The adsorption rate is faster in the first 5 min, slows down with increasing contact time and eventually reaches equilibrium. This is since more adsorption sites are available in the early stage. Later on, the repulsion between the solute and bulk phase causes difficulties to occupy the remaining sites [35].

3.3. Photocatalytic degradation of MO: Fig. 5*a* shows the result of the photocatalytic degradation of MO from different composites. After dark adsorption, the decolourisation rates of MO solution treated with Na–MMT, TiO_2–MMT, and $Bi_{20}TiO_{32}$–MMT are 13.35, 27.73, and 19.91%, respectively. After 120 min of UV treatment, the decolourisation rate of the MO solution containing Na–MMT remains constant. The decolourisation rates of the MO solutions treated with TiO_2–MMT and $Bi_{20}TiO_{32}$–MMT reach 87.11 and 98.50%, the decolourisation rates of $Bi_{20}TiO_{32}$–MMT increased by 11.39% compared with that of TiO_2–MMT. It is shown that the morphology and distribution of catalytic agent (TiO_2 or $Bi_{20}TiO_{32}$) in the composites play a major role in photocatalysis. On the one hand, the valence band (VB) orbital of bismuth titanate is formed by hybridising Bi 6s and O 2p, and the conduction band orbital is composed of Ti 3d. Orbital hybridisation moves VB up, and the bandgap decreases [36]. On the other hand, the Bi–O polyhedron may act as an electron donor, which promotes the transport of electrons to O_2 and reduces the recombination of hole–electron [37]. Also, it can be concluded from Table 1 that the degradation of MO with $Bi_{20}TiO_{30}$–MMT is an effective method by comparing the decolourisation rates of various materials under similar photocatalytic conditions as in this Letter.

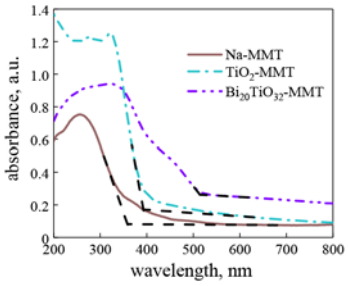

Fig. 3 *UV–Vis DRS spectra of as-prepared samples*

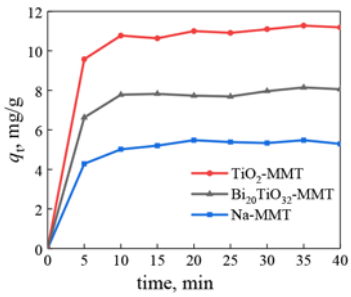

Fig. 4 *Adsorption curves of MO by different as-prepared samples*

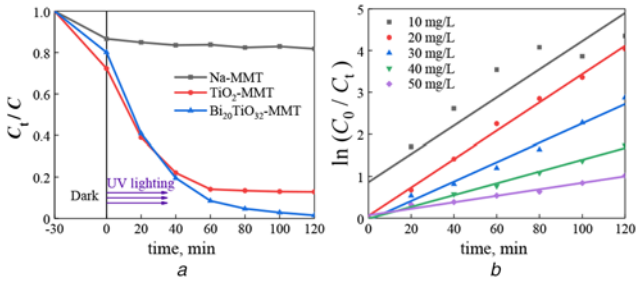

Fig. 5 *Curves of MO degradation*
a Photocatalytic degradation of MO over different composites
b Kinetic fit diagram

The pseudo-first-order kinetics equation (the following equation) was used to fit the kinetics of photocatalytic degradation of $Bi_{20}TiO_{32}$–MMT at different initial concentrations of the MO solution

$$\ln(C_0/C_t) = kt \tag{4}$$

where C_0 is the MO solution concentration after dark adsorption, mg/l; k is the pseudo-first-order reaction rate constant, min^{-1}.

It can be seen from Fig. 5*b* and Table 2 that the photocatalytic degradation of MO by $Bi_{20}TiO_{32}$–MMT complies with the

Table 1 MO decolouration rates (%) of various materials

Nanomaterial	Decolouration rates, %	Operation time, min	Sources
TiO_2	62.00	120	[38]
Bi^{3+}–TiO_2	91.43	120	[39]
C/La/Bi_2O_3–TiO_2	94.30	60	[40]
GO/TiO_2–Bi_2O_3	78.80	90	[41]
TiO_2(B) @$Bi_{20}TiO_{32}$	96.89	50	[42]
$Bi_{20}TiO_{32}$–MMT	98.50	120	This study

Table 2 Kinetic fit results

Initial concentration, mg/l	k	R^2
10	0.03365	0.83109
20	0.03381	0.99501
30	0.02307	0.98201
40	0.01405	0.99397
50	0.00775	0.96798

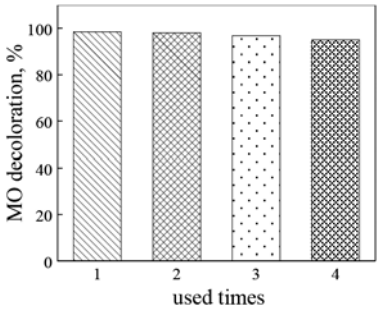

Fig. 6 *Stability testing of $Bi_{20}TiO_{32}$–MMT*

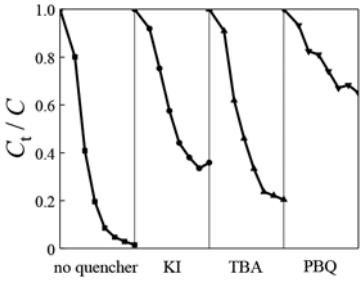

Fig. 7 *Effect of different quenchers on decolouration rate of MO*

pseudo-first-order kinetic equation. When the initial concentration of the MO solution is 10 mg/l, R^2 is <0.9. It is because when the concentration of MO is low, the adsorption ratio is relatively large, and the photocatalytic degradation is small. When the initial concentration of the MO solution increases from 20 to 50 mg/l, the pseudo-first-order reaction rate constant (k) decreases from 0.03381 to 0.00775 min^{-1}. Moreover, the reduction becomes larger. It shows that the synthesised $Bi_{20}TiO_{32}$–MMT has no significant effect on the treatment of a high concentration MO solution. When the MO concentration is more than 20 mg/l, more MO molecules are adsorbed on the surface of $Bi_{20}TiO_{32}$–MMT. Reducing the area excited by light affects the photocatalytic effect.

To study the stability of $Bi_{20}TiO_{32}$–MMT, it was washed, filtered, and dried before the usage. Photocatalytic degradation tests were performed under the same reaction conditions as described above. Fig. 6 shows that $Bi_{20}TiO_{32}$–MMT has excellent stability. After four reuses of $Bi_{20}TiO_{32}$–MMT, the decolourisation rate of MO only decreases by 3.45%, and the catalytic activity is slightly reduced. It may be due to the loss of $Bi_{20}TiO_{32}$–MMT during reusing. Also, the irreversible change of the dye molecule to the $Bi_{20}TiO_{32}$–MMT surface.

3.4. Photocatalytic mechanism: To better discover the photocatalytic mechanism of $Bi_{20}TiO_{32}$–MMT, the free radical masking test was used to explore the active substances which played a significant role in the photocatalytic process. The holes (h^+), hydroxyl radical, and superoxide radicals ($O_2^{-\cdot}$) were covered by potassium iodide (KI), tert-butyl alcohol (TBA), and p-benzoquinone (PBQ), respectively [43–45]. Fig. 7 shows that the decolourisation rate of MO after adding KI, TBA, and PBQ decreases by 34.38, 18.91, and 63.58%, respectively. It is shown that the active substances play a significant role in the degradation of MO are $O_2^{-\cdot}$ and h^+, especially $O_2^{-\cdot}$. The photocatalytic mechanism can be represented by Fig. 8. $Bi_{20}TiO_{32}$–MMT is excited by photons to generate h^+ and photo-induced electrons (e^-). $O_2^{-\cdot}$ are formed by the combination of e^- and oxygen dissolved in water. $O_2^{-\cdot}$ and h^+ then directly interact with MO to

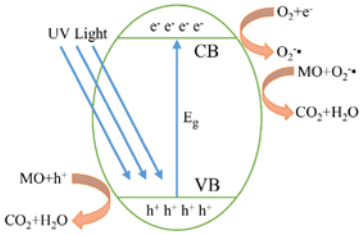

Fig. 8 *Photocatalytic mechanism of MO degradation by $Bi_{20}TiO_{32}$–MMT*

degrade it into small molecules such as water and carbon dioxide [46].

4. Conclusion: In summary, TiO_2–MMT and $Bi_{20}TiO_{32}$–MMT were successfully synthesised by the sol–gel method. Compared to Na–MMT and TiO_2–MMT, $Bi_{20}TiO_{32}$–MMT exhibited higher photocatalytic activity in degradation MO solution under the UV light irradiation. The decolourisation rate of the MO solution treated by $Bi_{20}TiO_{32}$–MMT could reach 98.50%. The improvement of photocatalytic efficiency was due to the decrease of the bandgap and the hole–electron recombination after the recombination of Bi_2O_3 and TiO_2. The photocatalytic mechanism experiment showed that substances such as $O_2^{-\cdot}$ and h^+ played a significant role in photocatalytic degradation. Besides, the cyclic use of $Bi_{20}TiO_{32}$–MMT showed that it had excellent stability and high mineralisation efficiency, which indicates that the synthesised $Bi_{20}TiO_{32}$–MMT has great potential in dye wastewater treatment.

5. Acknowledgments: This work was supported by the National Natural Science Foundation of China (grant no. 51464007), the Guizhou Provincial Science and Technology Department Joint Fund Project (grant no. 2015LH7684), and the Guizhou Science and Technology Plan Project (grant no. [2020]1Z045).

6 References

[1] Sun J., Hu Y., Bi Z., *ET AL.*: 'Simultaneous decolorization of azo dye and bioelectricity generation using a microfiltration membrane air-cathode single-chamber microbial fuel cell', *Bioresour. Technol.*, 2009, **100**, (13), pp. 3185–3192
[2] Martínez-Huitle C.A., Brillas E.: 'Decontamination of wastewaters containing synthetic organic dyes by electrochemical methods: a general review', *Appl. Catal. B*, 2009, **87**, (3), pp. 105–145
[3] Solanki K., Subramanian S., Basu S.: 'Microbial fuel cells for azo dye treatment with electricity generation: a review', *Bioresour. Technol.*, 2013, **131**, pp. 564–571
[4] Jiang P.: 'Study on the treatment technology of dye wastewater' (Ocean University of China, Qingdao, MA, 2012)
[5] Lau Y.-Y., Wong Y.-S., Teng T.-T., *ET AL.*: 'Coagulation–flocculation of azo dye acid orange 7 with green refined laterite soil', *Chem. Eng. J.*, 2014, **246**, pp. 383–390
[6] Pavithra K.G., Senthil Kumar P., Jaikumar V., *ET AL.*: 'Removal of colorants from wastewater: A review on sources and treatment strategies', *J. Ind. Eng. Chem.*, 2019, **75**, pp. 1–19
[7] Mei S., Gu J., Ma T., *ET AL.*: 'N-doped activated carbon from used dyeing wastewater adsorbent as a metal-free catalyst for acetylene hydrochlorination', *Chem. Eng. J.*, 2019, **371**, pp. 118–129
[8] Cui Y., Han J.: 'Current status of research and prospect on photocatalytic degradation of organic pollutants in water', *J. Fuel Chem. Technol.*, 2004, **32**, (1), pp. 123–128
[9] Zhou M., Yu J., Cheng B., *ET AL.*: 'Preparation and photocatalytic activity of Fe-doped mesoporous titanium dioxide nanocrystalline photocatalysts', *Mater. Chem. Phys.*, 2005, **93**, (1), pp. 159–163
[10] Zha Y., Meng F., Ding B., *ET AL.*: 'Facile hydrothermal synthesis of anatase TiO_2 hollow nanospheres with enhanced photocatalytic activity', *Russ. J. Phys. Chem. A.*, 2018, **92**, (9), pp. 1772–1776
[11] Qiu J., Sun X., Xing J., *ET AL.*: 'Preparation and photocatalytic activity of B, Ce Co-doped TiO_2 hollow fibers photocatalyst', *Russ. J. Phys. Chem. A*, 2014, **88**, (7), pp. 1236–1240

doi: 10.1049/mnl.2020.0127

[12] Zdravkov A.V., Gorbunova V.A., Volkova A.V., *ET AL.*: 'Preparation of photocatalytically active titanium dioxide doped with transition metal oxides', *Russ. J. Gen. Chem.*, 2018, **88**, (3), pp. 528–531

[13] Fard N.E., Fazaeli R.: 'Optimization of operating parameters in photocatalytic activity of visible light active Ag/TiO_2 nanoparticles', *Russ. J. Phys. Chem. A*, 2018, **92**, (13), pp. 2835–2846

[14] Allured B., DelaCruz S., Darling T., *ET AL.*: 'Enhancing the visible light absorbance of $Bi_2Ti_2O_7$ through Fe-substitution and its effects on photocatalytic hydrogen evolution', *Appl. Catal. B*, 2014, **144**, pp. 261–268

[15] Lin X., Lv P., Guan Q., *ET AL.*: 'Bismuth titanate microspheres: directed synthesis and their visible light photocatalytic activity', *Appl. Surf. Sci.*, 2012, **258**, (18), pp. 7146–7153

[16] Zhu X., Zhang J., Chen F.: 'Study on visible light photocatalytic activity and mechanism of spherical $Bi_{12}TiO_{20}$ nanoparticles prepared by low-power hydrothermal method', *Appl. Catal. B*, 2011, **102**, (1–2), pp. 316–322

[17] Cheng H., Huang B., Dai Y., *ET AL.*: 'Visible-light photocatalytic activity of the metastable $Bi_{20}TiO_{32}$ synthesized by a high-temperature quenching method', *J. Solid State Chem.*, 2009, **182**, (8), pp. 2274–2278

[18] Lomanovaa N.A., Tomkovicha M.V., Osipovb A.V., *ET AL.*: 'Synthesis of nanocrystalline materials based on the Bi_2O_3–TiO_2 system', *Russ. J. Gen. Chem.*, 2019, **89**, (10), pp. 1587–1594

[19] Kumar V., Sharma R., Kumar S., *ET AL.*: 'Enhancement in the photocatalytic activity of $Bi_2Ti_2O_7$ nanopowders synthesised via pechini vs co-precipitation method', *Ceram. Int.*, 2019, **45**, (16), pp. 20386–20395

[20] Fang G., Wang L., Zhang G., *ET AL.*: 'Rapid microwave-assisted sol–gel synthesis and exceptional visible light photocatalytic activities of $Bi_{12}TiO_{20}$', *Ceram. Int.*, 2018, **44**, (14), pp. 16388–16393

[21] Yang R.T., Baksh M.S.A.: 'Pillared clays as a new class of sorbents for gas separation', *AIChE J.*, 1991, **37**, (5), pp. 679–686

[22] Han L., Tuo B., Yang H., *ET AL.*: 'Adsorption mechanism of xanthate by zirconium pillared montmorillonite', *J. Chin. Ceram. Soc.*, 2017, **45**, (5), pp. 729–736

[23] Wang M.: 'Preparation and catalytic organic reaction of bentonite supported catalyst' (Qufu Normal University, Qufu, MA, 2010)

[24] Zhu J., Wang S., Wang J., *ET AL.*: 'Highly active and durable Bi_2O_3/TiO_2 visible photocatalyst in flower-like spheres with surface-enriched Bi_2O_3 quantum dots', *Appl. Catal. B*, 2011, **102**, (1), pp. 120–125

[25] Liu X., Lu X., Qiu J., *ET AL.*: 'Purification of low grade Ca–bentonite for iron ore pellets', *Adv. Mater. Res.*, 2012, **454**, pp. 237–241

[26] Bian Z., Zhu J., Wang S., *ET AL.*: 'Self-assembly of active Bi_2O_3/TiO_2 visible photocatalyst with ordered mesoporous structure and highly crystallized anatase', *J. Phys. Chem. C*, 2008, **112**, (16), pp. 6258–6262

[27] Malligavathy M., Iyyapushpam S., Nishanthi S.T., *ET AL.*: 'Remarkable catalytic activity of Bi_2O_3/TiO_2 nanocomposites prepared by hydrothermal method for the degradation of methyl orange', *J. Nanopart. Res.*, 2017, **19**, (4), p. 144

[28] Rengaraj S., Li X.Z., Tanner P.A., *ET AL.*: 'Photocatalytic degradation of methylparathion – an endocrine disruptor by Bi^{3+}-doped TiO_2', *J. Mol. Catal. A, Chem.*, 2006, **247**, (1), pp. 36–43

[29] Tanner P.A., Wong K.L., Liang Y.: 'Multiple phase production on doping Er^{3+} into α-Al_2O_3', *Chem. Phys. Lett.*, 2004, **399**, pp. 15–19

[30] Zhao X., Tuo B., Han L., *ET AL.*: 'Adsorption of Zn^{2+} on titanium intercalated montmorillonite', *Min. Metall. Eng.*, 2018, **38**, (6), pp. 151–155

[31] Hou Y., Wang M., Xu X., *ET AL.*: '$Bi_{20}tio_{32}$ nanocones prepared from Bi–Ti–O mixture by metalorganic decomposition method', *J. Cryst. Growth.*, 2002, **240**, (3), pp. 489–494

[32] Tauc J., Grigorovici R., Vancu A.: 'Optical properties and electronic structure of amorphous germanium', *Phys. Stat. Sol.*, 1966, **15**, (2), pp. 627–637

[33] Xiong Z., Zhao X.S.: 'Nitrogen-doped titanate-anatase core-shell nanobelts with exposed {101} anatase facets and enhanced visible light photocatalytic activity', *J. Am. Chem. Soc.*, 2012, **134**, (13), pp. 5754–5757

[34] Huo M., Guo H., Jiang Y., *ET AL.*: 'A facile method of preparing sandwich layered TiO_2 in between montmorillonite sheets and its enhanced UV-light photocatalytic activity', *J. Photochem. Photobiol. A*, 2018, **358**, pp. 121–129

[35] Patil S.P., Bethi B., Sonawane G.H., *ET AL.*: 'Efficient adsorption and photocatalytic degradation of rhodamine B dye over Bi_2O_3–bentonite nanocomposites: a kinetic study', *J. Ind. Eng. Chem.*, 2016, **34**, pp. 356–363

[36] Zhou J., Zou Z., Ray A.K., *ET AL.*: 'Preparation and characterization of polycrystalline bismuth titanate $Bi_{12}TiO_{20}$ and its photocatalytic properties under visible light irradiation', *Ind. Eng. Chem. Res.*, 2007, **46**, (3), pp. 745–749

[37] Kim H.G., Hwang D.W., Lee J.S.: 'An undoped, single-phase oxide photocatalyst working under visible light', *J. Am. Chem. Soc.*, 2004, **126**, (29), pp. 8912–8913

[38] Murcia J.J., Hidalgo M.C., Navio J.A., *ET AL.*: 'Correlation study between photo-degradation and surface adsorption properties of phenol and methyl orange on TiO_2 vs platinum-supported TiO_2', *Appl. Catal., B*, 2014, **150**, pp. 107–115

[39] Kang J., Yao L., Chen Y., *ET AL.*: 'Preparation and photocatalytic activities of Fe^{3+}–Bi^{3+} codoped TiO_2 nano-composite films', *Rare Met. Mater. Eng.*, 2012, **413**, pp. 587–590

[40] Zou H., Song M., Yi F., *ET AL.*: 'Simulated-sunlight-activated photocatalysis of methyl orange using carbon and lanthanum co-doped Bi_2O_3–TiO_2 composite', *J. Alloys Compd.*, 2016, **680**, pp. 54–59

[41] Chen C., Cao S., Long H., *ET AL.*: 'Highly efficient photocatalytic performance of graphene oxide/TiO_2–Bi_2O_3 hybrid coating for organic dyes and NO gas', *J. Mater. Sci., Mater. Electron.*, 2015, **26**, (6), pp. 3385–3391

[42] Hao P., Zhao Z., Tian J., *ET AL.*: 'Bismuth titanate nanobelts through a low-temperature nanoscale solid-state reaction', *Acta Mater.*, 2014, **62**, pp. 258–266

[43] Liu C., Wu Q., Ji M., *ET AL.*: 'Constructing Z-scheme charge separation in 2D layered porous BiOBr/graphitic C_3N_4 nanosheets nanojunction with enhanced photocatalytic activity', *J. Alloys Compd.*, 2017, **723**, pp. 1121–1131

[44] Liu C., Zhu H., Zhu Y., *ET AL.*: 'Ordered layered N-doped $KTiNbO_5$/g-C_3N_4 heterojunction with enhanced visible light photocatalytic activity', *Appl. Catal. B*, 2018, **228**, pp. 54–63

[45] Liu C., Xu Q., Zhang Q., *ET AL.*: 'Layered BiOBr/Ti_3C_2 MXene composite with improved visible-light photocatalytic activity', *J. Mater. Sci.*, 2019, **54**, (3), pp. 2458–2471

[46] Fu D., Zhang L., Xie R., *ET AL.*: 'Fabrication of novel rGO/$Bi_{20}TiO_{32}$ heterojunction for enhanced visible-light photocatalytic activity', *J. Photochem. Photobiol. A*, 2016, **329**, pp. 18–25